

Dative Epitaxy of Commensurate Monocrystalline Covalent van der Waals Moiré Supercrystal

Mengying Bian, Liang Zhu, Xiao Wang, Junho Choi, Rajesh V. Chopdekar, Sichen Wei, Lishu Wu, Chang Huai, Austin Marga, Qishuo Yang, Yuguang C. Li, Fei Yao, Ting Yu, Scott A. Crooker, Xuemei M. Cheng, Renat F. Sabirianov, Shengbai Zhang, Junhao Lin,* Yanglong Hou,* and Hao Zeng*

Realizing van der Waals (vdW) epitaxy in the 1980s represents a breakthrough that circumvents the stringent lattice matching and processing compatibility requirements in conventional covalent heteroepitaxy. However, due to the weak vdW interactions, there is little control over film qualities by the substrate. Typically, discrete domains with a spread of misorientation angles are formed, limiting the applicability of vdW epitaxy. Here, the epitaxial growth of monocrystalline, covalent Cr_5Te_8 2D crystals on monolayer vdW WSe_2 by chemical vapor deposition is reported, driven by interfacial dative bond formation. The lattice of Cr_5Te_8 , with a lateral dimension of a few tens of micrometers, is fully commensurate with that of WSe_2 via $3 \times 3 (\text{Cr}_5\text{Te}_8)/7 \times 7 (\text{WSe}_2)$ supercell matching, forming a single-crystalline moiré superlattice. This work establishes a conceptually distinct paradigm of thin-film epitaxy, termed “dative epitaxy”, which takes full advantage of covalent epitaxy with chemical bonding for fixing the atomic registry and crystal orientation, while circumventing its stringent lattice matching and processing compatibility requirements; conversely, it ensures the full flexibility of vdW epitaxy, while avoiding its poor orientation control. Cr_5Te_8 2D crystals grown by dative epitaxy exhibit square magnetic hysteresis, suggesting minimized interfacial defects that can serve as pinning sites.

1. Introduction

2D heterostructures obtained by stacking van der Waals (vdW) layers have attracted intense interest for fundamental research and applications in electronics,^[1] optoelectronics,^[2] spintronics,^[3] and valleytronics.^[4] In particular, moiré superlattices achieved by aligning or twisting individual 2D layers offer an additional degree of freedom for manipulating the electronic structure. It is well-known that correlated insulating states, superconductivity, magnetism, and topological quantum states can emerge in twisted bilayer graphene,^[5] graphene/hexagonal boron nitride,^[6] and transition metal dichalcogenide (TMD) moiré superlattices.^[7] Moiré superlattice exciton states and interlayer valley excitons were also observed in TMD heterostructures such as WSe_2/WS_2 and $\text{MoSe}_2/\text{WSe}_2$, respectively.^[8] However, the conventional

M. Bian, Y. Hou
Beijing Key Laboratory for Magnetoelectric Materials and Devices
Beijing Innovation Center for Engineering Science and Advanced Technology
School of Materials Science and Engineering
Peking University
Beijing 100871, China
E-mail: hou@pku.edu.cn

M. Bian, C. Huai, A. Marga, H. Zeng
Department of Physics
University at Buffalo
State University of New York
Buffalo, NY 14260, USA
E-mail: haozeng@buffalo.edu

L. Zhu, Q. Yang, J. Lin
Department of Physics and Shenzhen Key Laboratory of Advanced Quantum Functional Materials and Devices
Southern University of Science and Technology
Shenzhen 518055, China
E-mail: linjh@sustech.edu.cn

 The ORCID identification number(s) for the author(s) of this article can be found under <https://doi.org/10.1002/adma.202200117>.

X. Wang, X. M. Cheng
Physics Department
Bryn Mawr College
Bryn Mawr, PA 19010, USA

J. Choi, S. A. Crooker
National High Magnetic Field Laboratory
Los Alamos National Laboratory
Los Alamos, NM 87545, USA

R. V. Chopdekar
Advanced Light Source
Lawrence Berkeley National Laboratory
Berkeley, CA 94720, USA

S. Wei, F. Yao
Department of Materials Design and Innovation
University at Buffalo
The State University of New York
Buffalo, NY 14260, USA

L. Wu, T. Yu
Division of Physics & Applied Physics
School of Physical and Mathematical Sciences
Nanyang Technological University
Singapore 637371, Singapore

DOI: 10.1002/adma.202200117

exfoliation and stacking approach lacks scalability for practical applications.

Recently, 2D vdW heterostructures have been realized by chemical vapor deposition (CVD), such as graphene/hexagonal boron nitride,^[9] and TMD heterostructures (e.g., WS₂/MoS₂, SnS₂/MoS₂, and NbTe₂/WSe₂).^[10] vdW epitaxy overcomes the constraints of lattice matching and processing compatibility requirements in conventional covalent heteroepitaxy.^[11] It is particularly suitable for synthesizing 2D heterostructures owing to the atomically smooth and dangling-bond-free vdW surface. However, because vdW surfaces are chemically inactive, chemical or plasma treatment may be needed to facilitate nucleation, which leads to a defective interface.^[12] Moreover, limited success has been achieved for vdW epitaxy of continuous thin films of materials with 3D crystal structures on vdW substrates. Instead, discrete nanowires or domains with a spread of misorientation alignment were typically obtained.^[13] This is because the weak vdW interaction and the resulting energy landscape as a function of the in-plane orientation angle may not exhibit clearly defined minima, required for high-quality epitaxy.^[13,14]

In this work, we report dative epitaxy of a high-quality single-crystalline layer of 3D-bonded material on a 2D vdW template with large lattice mismatch. This unexplored regime of epitaxy exploits the bonding duality at the interface to realize epitaxial growth: the weak vdW interactions allow facile surface diffusion of precursor molecules for the growth of large area continuous layers, while the formation of dative bond (a special covalent bond where the bonding electrons derive from the same atom) fixes atomic registry and crystal orientation. Specifically, we focus on the 2D heterostructure of Cr₅Te₈/WSe₂, where Cr₅Te₈ is a non-vdW ferromagnet that can be considered as Cr atoms self-intercalated in between the CrTe₂ layers^[15] (as shown schematically in Figure S1a in the Supporting Information). First, a large-scale WSe₂ monolayer millimeter in size was grown on a sapphire or Si/SiO₂ substrate by CVD. Highly aligned 2D Cr₅Te₈ crystals with thicknesses down to a single unit cell and yet sizes of tens of micrometers were then achieved by dative epitaxy, with WSe₂ as the vdW template. As a result, a globally commensurate, monocrystalline 3 × 3/7 × 7 Cr₅Te₈/WSe₂ moiré supercrystal is achieved, which differs from conventional moiré superlattices with spatially varying rigid moiré patterns^[16] or local commensurate domain reconstruction.^[17] Three decades after the realization of vdW epitaxy,^[11a] our work redefines the scope and applicability of epitaxy with unprecedented opportunities for applications.

2. Results and Discussion

A schematic of the growth process of 2D Cr₅Te₈/WSe₂ moiré superlattices is shown in Figure 1a, which consists of monomer adsorption, desorption, and surface diffusion. Further details of the growth process are shown in the Experimental Section. CVD grown monolayer WSe₂ with lateral dimensions of 100–2000 μm, used as templates for the growth of Cr₅Te₈/WSe₂ heterostructures, are shown in Figure 1b,c.^[18] A typical optical microscope image of the heterostructures is shown in Figure 1d. Strikingly, all the Cr₅Te₈ crystals grown on a single monolayer WSe₂ are self-aligned, with one of their edges oriented either parallel or at a 60° angle to one of the edges of WSe₂, in contrast to the randomly oriented Cr₅Te₈ crystals grown directly on sapphire (Figure S2a, Supporting Information). This strongly suggests that the Cr₅Te₈ crystals grow epitaxially on WSe₂. While monolayer WSe₂ are randomly oriented, the orientations of the Cr₅Te₈ crystals align with individual WSe₂ crystals, suggesting the dominant role of monolayer WSe₂ in the epitaxial growth. Therefore, such vdW templates also allow the synthesis of highly oriented 2D Cr₅Te₈ crystals independent of substrates, as evidenced by samples grown on amorphous SiO₂ substrates (Figure S2g,h, Supporting Information).

Optical microscopy images of Cr₅Te₈/WSe₂ heterostructures with relatively thick (~10 nm) and thin (1.4–2.8 nm) Cr₅Te₈ crystals are shown in Figure 1e,f, respectively. They were achieved by controlling the distance between the CrCl₃ precursor and the substrate. The atomically thin Cr₅Te₈ crystals in Figure 1f exhibit extremely weak contrast. To help discern these crystals from the substrate, the boundaries of these crystals are highlighted by the dashed lines (the same image with enhanced contrast is shown in Figure S2b in the Supporting Information). A group of one unit cell thick, aligned Cr₅Te₈ crystals on WSe₂ are further shown by the atomic force microscopy (AFM) image in Figure 1g and Figure S2d (Supporting Information).

The *a* lattice constants of freestanding WSe₂ and Cr₅Te₈ are 3.33 and 790 Å, respectively. Conventional vdW epitaxy mechanism implies that with ~16% lattice mismatch, defined as $(a_{\text{Cr}_5\text{Te}_8} - 2a_{\text{WSe}_2}) / a_{\text{Cr}_5\text{Te}_8}$, the Cr₅Te₈ and WSe₂ would form incommensurate moiré superlattices.^[19] Indeed, a moiré pattern can be clearly seen in the atomically resolved plane-view high angle annular dark field scanning transmission electron microscopy (HAADF-STEM) image in Figure 2a. However, the strictly periodic moiré pattern suggests that the Cr₅Te₈ and WSe₂ lattices are commensurate. The fast Fourier transform (FFT) pattern (Figure 2b) reveals three distinct sets of diffraction spots with sixfold symmetry, marked by yellow, red, and blue circles, respectively. The lattice spacing of the diffraction spots marked by yellow circles is 2.88 Å, which is consistent with the measured (100) lattice spacing of monolayer WSe₂. The diffraction spots marked with red circles show identical orientation with that of the WSe₂, with a lattice spacing of 3.36 Å in accordance with the Cr₅Te₈ (200) planes, which reduces by ~2% from the value of freestanding Cr₅Te₈.^[20] The inner, red-circled diffraction spots with a larger periodicity (6.72 Å) representing those ordered, self-intercalated Cr atoms is a structural fingerprint of trigonal Cr₅Te₈. Interestingly, the innermost diffraction spots highlighted by blue circles indicate a lattice spacing of 11.6 Å, which belongs to neither WSe₂ nor Cr₅Te₈ alone,

Y. C. Li
Department of Chemistry
University at Buffalo
The State University of New York
Buffalo, NY 14260, USA
R. F. Sabirianov
Department of Physics
University of Nebraska–Omaha
Omaha, NE 68182, USA
S. Zhang
Department of Physics
Rensselaer Polytechnic Institute
Troy, NY 12180, USA

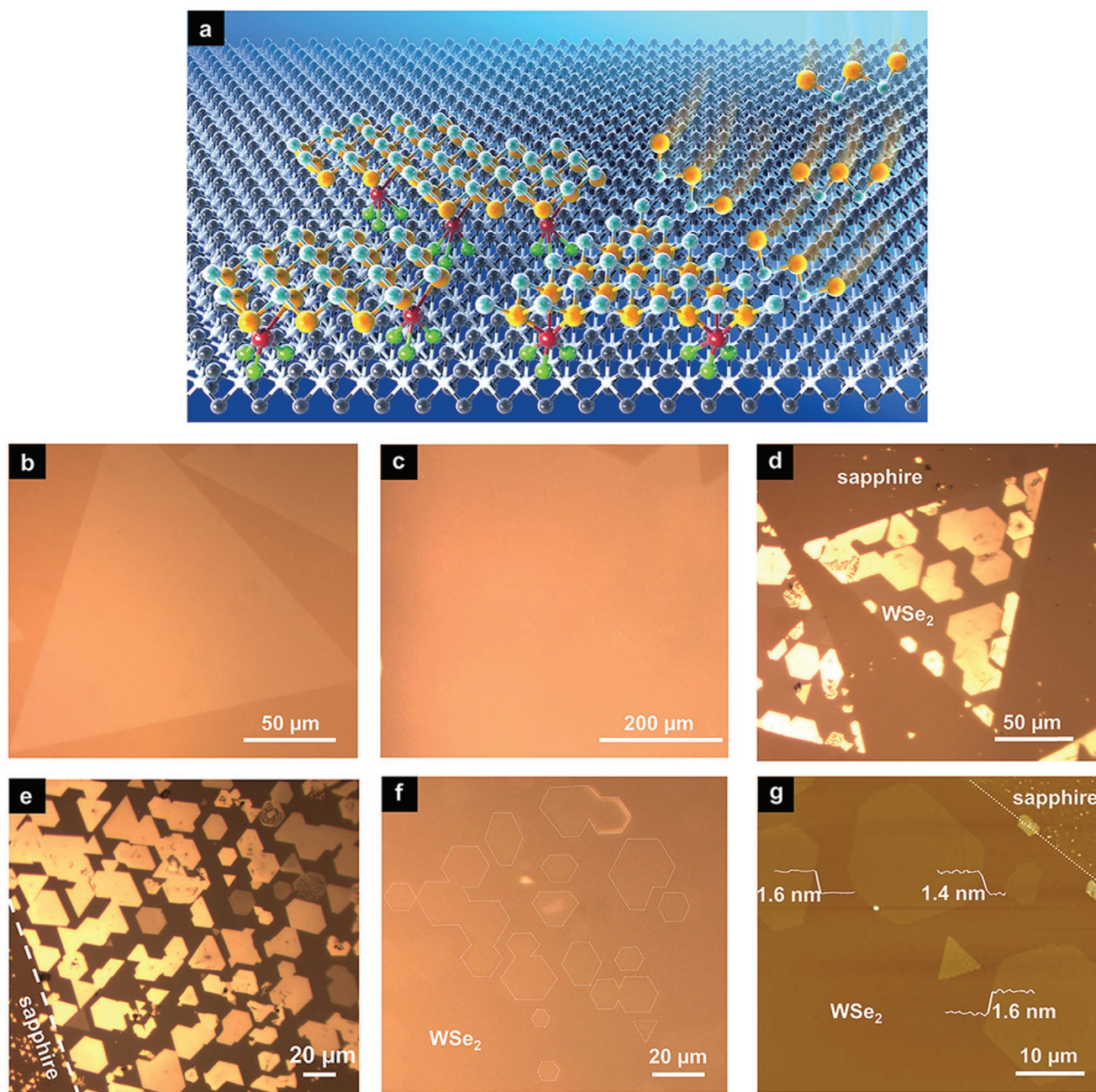


Figure 1. Epitaxial growth process of $\text{Cr}_5\text{Te}_8/\text{WSe}_2$ heterostructures, optical and atomic force microscopy images of WSe_2 and $\text{Cr}_5\text{Te}_8/\text{WSe}_2$ heterostructures. a) A schematic of the epitaxial growth processes of 2D $\text{Cr}_5\text{Te}_8/\text{WSe}_2$ heterostructures, showing monomer adsorption, desorption, and diffusion. It also shows chemical bonding between interfacial Cr (red) and Se atoms (green). b,c) Optical microscopy images of monolayer WSe_2 of sizes of $\approx 200 \mu\text{m}$ (b) and $\approx 1 \text{ mm}$ (c); d) 2D $\text{Cr}_5\text{Te}_8/\text{WSe}_2$ heterostructures; and e,f) highly aligned Cr_5Te_8 crystals with a thickness of $\approx 10 \text{ nm}$ (e) and $1.4\text{--}2.8 \text{ nm}$ (the dashed lines serve as visual aids to discern the boundaries of 2D crystals) (f) on a single monolayer WSe_2 . g) An AFM image of an area of one unit cell thick Cr_5Te_8 crystals; the dashed line shows the boundary between monolayer WSe_2 and sapphire substrate.

suggesting that it originates from the periodicity of the moiré superlattice of the $\text{Cr}_5\text{Te}_8/\text{WSe}_2$ heterostructure. The individual lattices of Cr_5Te_8 and WSe_2 are resolved by inverse FFT (iFFT) of the corresponding filtered diffraction spots (Figure S3, Supporting Information), showing hexagonal lattices of both WSe_2 and Cr_5Te_8 aligned in identical orientation, as seen in Figure 2c,d, respectively.

An atomic model of the $\text{Cr}_5\text{Te}_8/\text{WSe}_2$ heterostructure based on iterative refinements from HAADF-STEM image analysis and first principle calculations is shown in Figure 2e, where a 3×3 Cr_5Te_8 supercell is commensurate with the 7×7 WSe_2 supercell. To generate the larger periodicity with sixfold symmetry that reproduces the observed moiré diffraction pattern shown by the blue circles in Figure 2b, the model requires the number

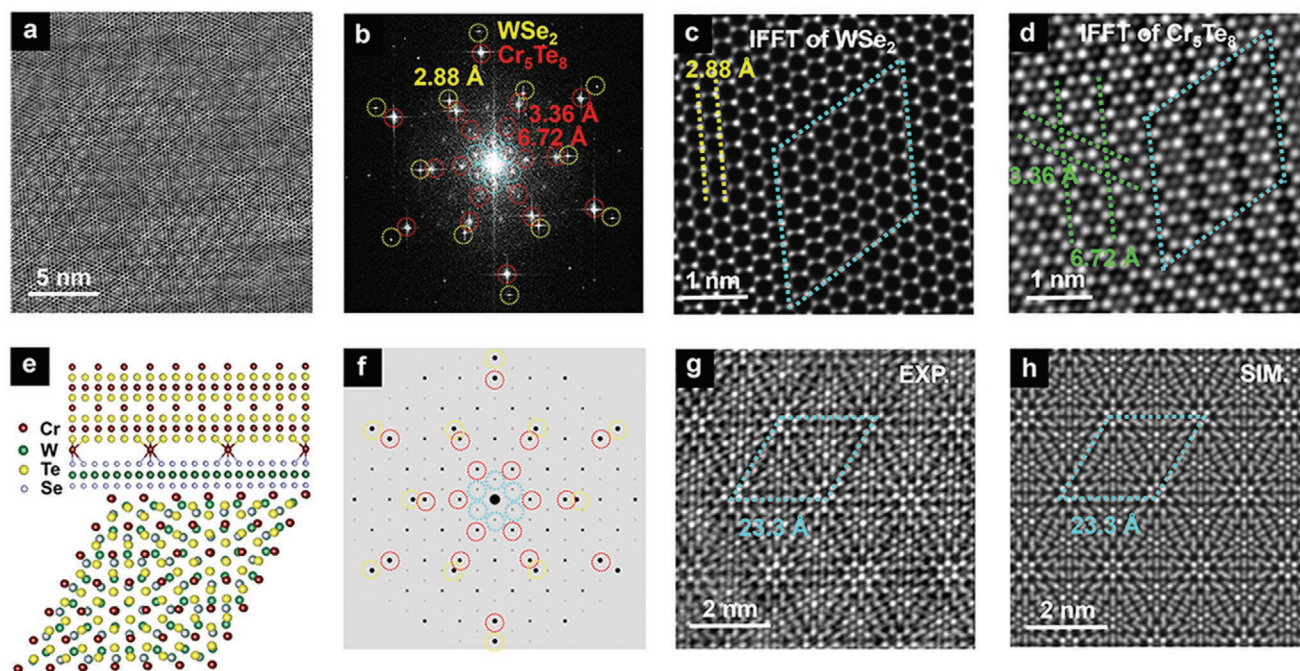


Figure 2. HAADF-STEM analysis of the $\text{Cr}_5\text{Te}_8/\text{WSe}_2$ moiré superlattice. a) Atomic-resolution HAADF-STEM image showing the moiré pattern of the $\text{Cr}_5\text{Te}_8/\text{WSe}_2$ heterostructure. b) FFT pattern obtained from (a). The diffraction spots marked by yellow circles: WSe_2 (100); outer red circles: Cr_5Te_8 (200); inner red circles: self-intercalated Cr atoms matched to trigonal Cr_5Te_8 ; blue circles: the moiré superlattice. c,d) iFFT images of identically oriented WSe_2 (c) and Cr_5Te_8 (d) lattices obtained from (b). e) Side view along (210) and top view of the atomic model of the $\text{Cr}_5\text{Te}_8/\text{WSe}_2$ superlattice. f) Simulated diffraction patterns obtained from the atomic model, matching that in (b). g) Experimental and h) simulated HAADF-STEM images showing identical moiré superlattice of $\text{Cr}_5\text{Te}_8/\text{WSe}_2$.

of interfacial Cr atoms to be reduced to 3 per supercell from 9 self-intercalated in the interior of Cr_5Te_8 , suggesting interfacial reconstruction. In slight variations of the atomic model, either without interfacial Cr or with 9 interfacial Cr per supercell, the moiré superlattice diffraction pattern is noticeably missing since it is symmetry forbidden (Figure S5, Supporting Information). This further confirms that the reconstructed interface with suitable Cr occupation is a necessary condition for the observed moiré diffraction pattern and the commensurate moiré superlattice. As can be seen from Figure 2f, the simulated diffraction pattern matches well with that of Figure 2b. The high-resolution STEM image reveals the perfectly commensurate moiré superlattice with a lattice constant of 23.3 Å, as shown in Figure 2g. The simulated STEM image (Figure 2h) based on the atomic model reproduces the moiré pattern observed. The surprising observation of the commensurate moiré superlattice is contradictory to the common knowledge of weak vdW interactions; instead, it suggests the presence of chemical bonding between Cr_5Te_8 and WSe_2 .

First principle calculations were carried out to understand the atomic structure, charge transfer, and chemical bonding at the $\text{Cr}_5\text{Te}_8/\text{WSe}_2$ interface. In bulk, the self-intercalated Cr atoms are coordinated with 6 Te atoms arranged on the corners of a triangular prism, as seen in Figure 2e. The interfacial Cr atoms have excess electrons due to the reduced coordination (losing 3 nearest Te neighbors comparing to the bulk). After forming the heterostructure, the crystal symmetry is further lowered with these interfacial Cr atoms coordinating to Se atoms on the WSe_2 side, forming a Te–Cr–Se Janus interface.

Figure 3a compares the site-decomposed partial density of states (DOS) of interfacial Cr (left panel) and Se (right panel) sp states for isolated Cr_5Te_8 and WSe_2 monolayer (red curves) with those of $\text{WSe}_2/\text{Cr}_5\text{Te}_8$ heterostructure (black curves). As can be seen from the change of DOS of Cr in the left panel, the majority spin state peak near the Fermi level (the red peak) is suppressed. Accompanying the suppression, a band at ≈ -7 to -4 eV emerges. The emergence of this low-lying Cr band is a result of hybridization with the Se sp states, whose energy is also lowered due to the hybridization, as can be seen in the right panel.

One can understand the above results based on a level repulsion picture in Figure 3b: the two states shown in red color are the interfacial Cr and Se sp states before Cr_5Te_8 and WSe_2 form the heterostructure. When forming the heterostructure, the Cr and Se sp states hybridize: the high-lying Cr sp state is pushed up in energy forming an antibonding state, so its spectra weight near the Fermi level is suppressed, while the low-lying Se sp state is pushed down forming a bonding state in line with the result in the right panel in Figure 3a. As this is a hybridization, Cr also takes a significant share in the newly formed low-lying state, as evidenced by the band at ≈ -7 to -4 eV in the left panel in Figure 3a. Interestingly, after the hybridization, the antibonding state is pushed up to be above the WSe_2 conduction band edge, resulting in electron transfer from the interfacial Cr to WSe_2 conduction band to reduce system energy.

Figure 3c shows the differential (deformation) charge density $\Delta\rho$, which reveals a bonding-state charge accumulation in-between the interfacial Cr and Se atoms. Based on the

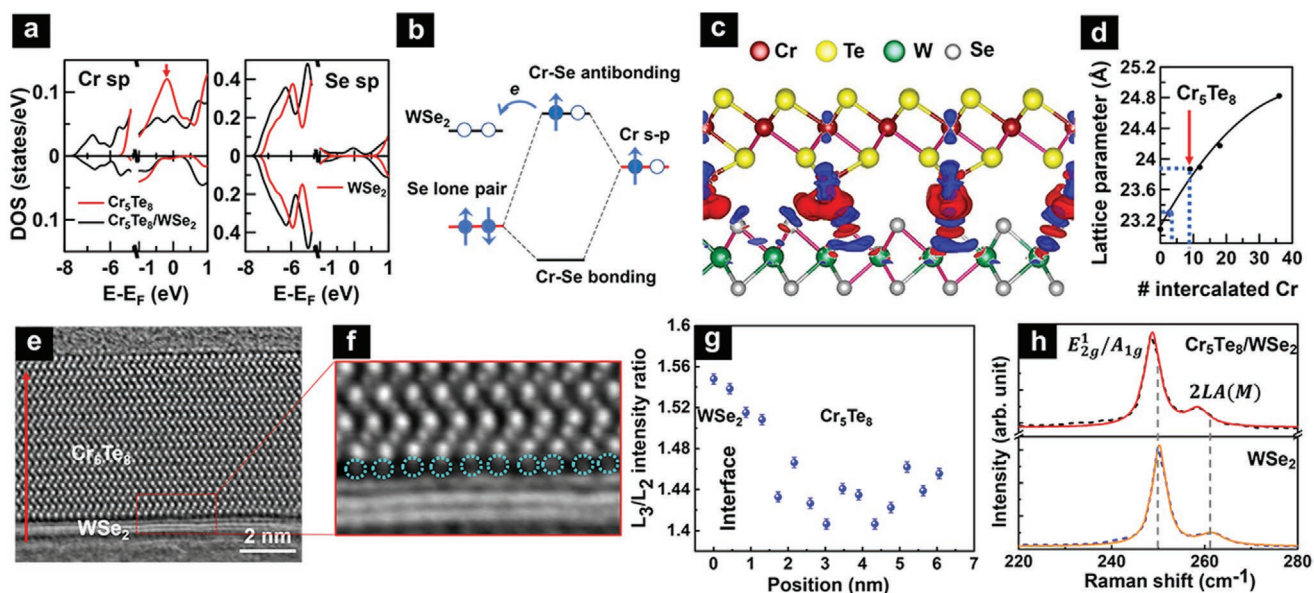


Figure 3. Atomic and electronic structure of the $\text{Cr}_5\text{Te}_8/\text{WSe}_2$ interface. a) Site-decomposed partial DOS of interfacial Cr (left) and Se (right) sp states for individual Cr_5Te_8 , WSe_2 (red curves), and $\text{WSe}_2/\text{Cr}_5\text{Te}_8$ (black curves). b) A schematic diagram illustrating the dative bond formation process. c) The c -axis projected differential charge density $\Delta\rho$ profile along the Te–Cr–Se–W direction. d) Calculated lattice spacing of CrTe_x as a function of self-intercalated Cr number. e) Cross-sectional iDPC image of the $\text{Cr}_5\text{Te}_8/\text{WSe}_2$ heterostructure. The red arrow in (e) indicates the EELS line scan direction; the red box is the area shown in (f). f) A magnified image of the area indicated in (e). The circles mark the atomic columns with weak contrast, which are attributed to interfacial Cr atoms. g) The integrated intensity ratio between Cr L_3 and L_2 edges measured by EELS as a function of position from WSe_2 to Cr_5Te_8 along the red arrow direction in (e). The error bars represent statistical uncertainty of the mean value. h) Raman spectra of monolayer WSe_2 and $\text{Cr}_5\text{Te}_8/\text{WSe}_2$ heterostructure. Black dashed lines: data; red and orange lines: fittings using Lorentzian function.

Bader analysis^[21] (see Table S2 in the Supporting Information), the total amount of charge accumulated is about 1 electron per supercell. The interfacial Cr–Se bond length of 2.88 Å is noticeably longer than the 2.56 Å for Cr_2Se_3 . The interfacial binding energy of ≈ 1 eV/Cr is an order of magnitude larger than a typical vdW binding but is only half of the usual Cr–Se covalent bond. These results point consistently to the formation of dative bonds at the interface,^[13] which originates from Coulomb attraction between anion lone pairs (i.e., the doubly occupied nonbonding states of interfacial Se atoms) and the empty orbitals of the metal cations (i.e., the nearly empty Cr sp states upon electron transfer to the WSe_2 conduction band) and is intermediate in strength between the vdW binding and covalent bond. The formation of the dative bonds weakens adjacent Cr–Te and W–Se bonds, e.g., the W–Se bond length increases from 2.545 to 2.550 Å.

The formation of directional dative bonds is ultimately responsible for fixing the atomic registry and orientation of the Cr_5Te_8 2D crystals on WSe_2 monolayer. It represents a new regime of thin film epitaxy that is distinctly different from either a conventional 3D epitaxy with strong covalent bond or a standard vdW epitaxy. We expect that dative epitaxy can be generally applicable to other covalent materials on vdW templates. The conditions for the formation of dative bonds at the interface are the presence of metal cations that can donate electrons and lone pairs that exist in many vdW materials such as transition metal chalcogenides. It has been shown previously that for two materials with a large lattice mismatch, epitaxy can be achieved by domain matching.^[19] To minimize the residue strain, the supercell size is approximately a least common

multiple of the lattice parameter of each material dictated by the mismatch. Dative epitaxy of different materials is expected to follow such matching conditions.

Figure 3d plots the calculated bulk lattice parameters of CrTe_x (represented by the superlattice parameter) as a function of the number of self-intercalated Cr atoms. It can be seen that the lattice parameter shrinks monotonically with decreasing the number of Cr atoms, e.g., from 23.8 Å for 9 Cr in Cr_5Te_8 to 23.3 Å for 3 Cr. Note that 3 Cr is identical to the interfacial Cr number in the atomic model that reproduces the moiré diffraction pattern, and 23.3 Å is the measured moiré superlattice parameter that is exactly 7 times the lattice constant of monolayer WSe_2 . It is remarkable that nature optimizes dative bond formation to remove the $\approx 2\%$ interfacial strain that would appear otherwise for the epitaxial growth.

In conventional vdW heterostructures with large lattice mismatch, either incommensurate superlattices with spatially varying moiré patterns^[16] or local commensurate domain reconstruction were observed.^[17] In conventional covalent heteroepitaxy, on the other hand, interfacial strain would lead to defects such as dislocations. For the $\text{Cr}_5\text{Te}_8/\text{WSe}_2$ system, however, nature optimizes the atomic structure with just the right number of dative bonds at the interface. This allows nearly strain-free commensurate moiré superlattices over the entire 2D heterostructure with minimum density of interfacial defects. As evidenced by the HAADF-STEM images taken at different spots of a single $\text{Cr}_5\text{Te}_8/\text{WSe}_2$ heterostructure (Figure S4, Supporting Information), identical, perfectly commensurate moiré patterns were observed across the heterostructure, suggesting that the $\text{Cr}_5\text{Te}_8/\text{WSe}_2$ is a monocrystalline moiré

Table 1. Raman peak positions of monolayer WSe₂ and Cr₅Te₈/WSe₂.

WSe ₂ E _{2g} ¹ /A _{1g} [cm ⁻¹]	Cr ₅ Te ₈ /WSe ₂ E _{2g} ¹ /A _{1g} [cm ⁻¹]	ΔνE _{2g} ¹ /A _{1g} [cm ⁻¹]	WSe ₂ 2LA(M) [cm ⁻¹]	Cr ₅ Te ₈ /WSe ₂ 2LA(M) [cm ⁻¹]	Δν 2LA(M) [cm ⁻¹]
250.21 ± 0.04	248.93 ± 0.12	1.3	261.63 ± 0.08	259.24 ± 0.18	2.4

super-crystal. To our knowledge, such a monocrystalline moiré super-crystal has not been reported before and provides strong evidence for the proposed dative epitaxy mechanism.

The cross-section of a relatively thick (≈7 nm) Cr₅Te₈ layer grown on WSe₂ was imaged by HAADF-STEM to reveal atomic details of the interface (atomically thin Cr₅Te₈/WSe₂ got oxidized during cross-sectional sample preparation). To reveal the position of Cr atoms that are much lighter than Te, integrated differential-phase contrast (iDPC) imaging technique was employed. As can be seen in Figure 3e, the cross-section of Cr₅Te₈ viewed along (100) direction matches well with the atomic model in Figure S1a (Supporting Information). Atomic columns with substantially weaker contrast inside the vdW-like gap can be seen from the zoomed-in view in Figure 3f, which is attributed to the reduced number of interfacial Cr atoms, consistent with the atomic model matching diffraction and theoretical predictions. The local valence states of Cr atoms across the interface were mapped using the integrated intensity ratio of the electron energy loss spectroscopy (EELS) L₃ and L₂ excitation peaks (the so-called “white line ratio”).^[22] As shown in Figure 3g, the Cr L₃/L₂ ratio increases toward the interface and becomes substantially larger than the value in the Cr₅Te₈ interior, indicating a lower Cr valence state near the interface (individual EELS spectrum at the bulk and interface is provided in Figure S6 in the Supporting Information). This is because

after dative bond formation and electron donation, these interfacial Cr atoms still possess excessive charge due to lower coordination.

The predicted weakening of W–Se bonds in WSe₂ was further investigated by Raman spectroscopy. As seen from the bottom panel in Figure 3h, a strong peak at ≈250 cm⁻¹ and a weak shoulder at ≈260 cm⁻¹ are observed for monolayer WSe₂, which can be attributed to the degenerate out-of-plane A_{1g} and in-plane E_{2g}¹ phonon modes of WSe₂, and a second-order Raman mode due to longitudinal acoustic (LA) phonons at the M point in the Brillouin zone labeled as 2LA(M), respectively.^[23] These modes are also observed for the Cr₅Te₈/WSe₂ moiré superlattice. However, both peaks showed a small but measurable redshift. The average Raman peak positions measured at 9 different spots each for WSe₂ and Cr₅Te₈/WSe₂ are shown in Table 1 (all spectra and fittings are shown in Figure S7a,b and Table S1 in the Supporting Information). A redshift (Δν) of 1.3 cm⁻¹ for the E_{2g}¹/A_{1g} mode and 2.4 cm⁻¹ for the 2LA(M) mode were observed, confirming the predicted W–Se bond softening due to dative bond formation.

Dative epitaxy enables nearly strain-free epitaxial growth of discrete monocrystalline 2D Cr₅Te₈ crystals on a single monolayer WSe₂, which should lead to extremely low density of interfacial defects. The out-of-plane magnetic hysteresis of single 2D Cr₅Te₈ crystals was measured by reflective magnetic

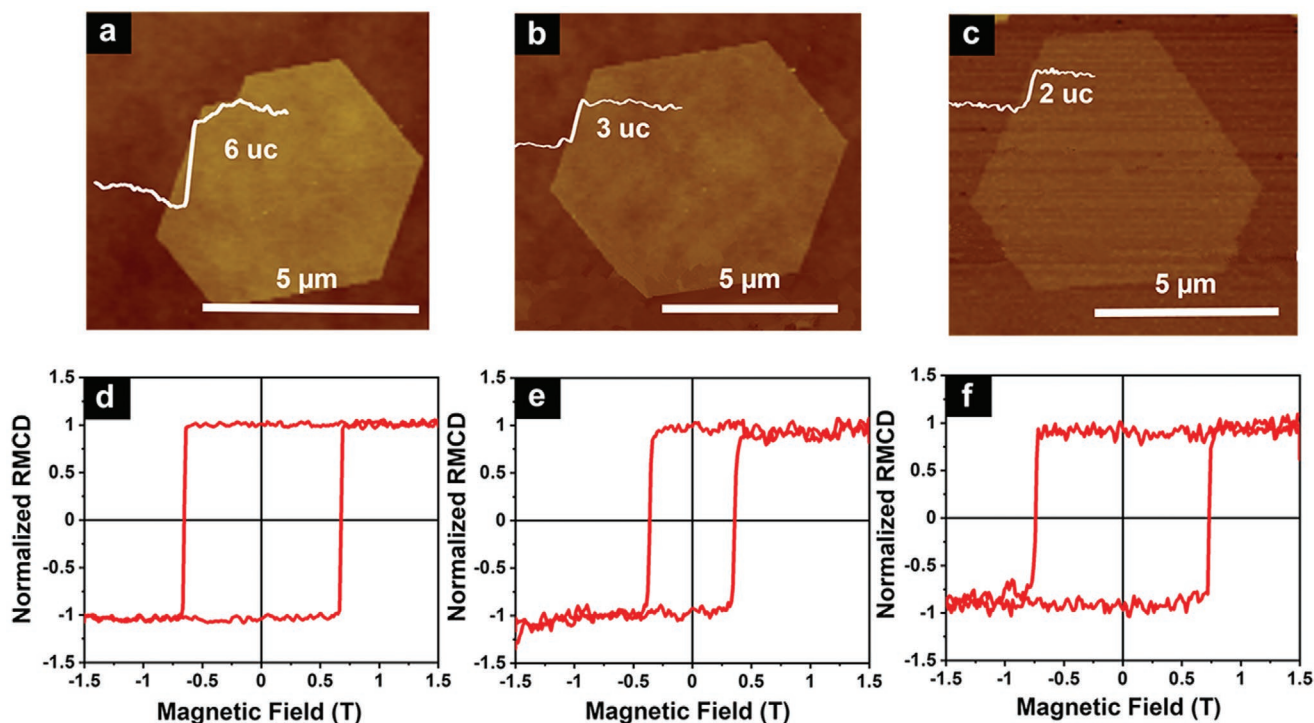


Figure 4. RMCD measurements of Cr₅Te₈ single flakes grown on WSe₂. a–c) AFM images of Cr₅Te₈ crystals grown on WSe₂ and d–f) the corresponding RMCD hysteresis loops measured at 5 K.

circular dichroism (RMCD), which is used to infer the crystallinity of Cr₅Te₈. Shown in Figure 4a–c are three representative 2D Cr₅Te₈ crystals with thicknesses of 8.4 nm (6 unit cells), 4.5 nm (3 unit cells), and 2.6 nm (2 unit cells), respectively. The magnetic hysteresis loops for the three crystals measured at 5 K are shown in Figure 4d–f. All three samples exhibit square hysteresis loops, with sharp transitions at the coercive fields (H_C), and unity remanence at zero field. H_C are 0.66, 0.36, and 0.74 T for 6, 3, and 2 unit cell thick crystals, respectively, which are noticeably smaller than the expected anisotropy field,^[24] suggesting that the magnetization reversal proceeds by nucleation (e.g., at a sharp corner) followed by domain wall motion. The nearly perfect square hysteresis suggests nearly absence of domain wall pinning by defects, and thus once a magnetic domain is nucleated, the domain wall can propagate freely. On the other hand, the reported magnetic hysteresis of Cr_xTe_{1-x} nanoplates on covalent substrates shows skewed loops with a broad switching field distribution.^[25] This might imply the presence of interfacial pinning sites. This comparison suggests that 2D Cr₅Te₈ crystals obtained by dative epitaxy do possess superior crystal quality and magnetic properties. For one unit cell thick Cr₅Te₈ crystals, however, no RMCD signal can be detected. The lack of magnetic signal may be due to surface oxidation.

3. Conclusion

Cr₅Te₈/WSe₂ moiré supercrystals have been achieved by dative epitaxy of covalent 2D Cr₅Te₈ crystal on monolayer WSe₂. The Cr–Se dative bond formation at the interface drives the epitaxial growth of highly aligned 2D Cr₅Te₈ crystals. The dative epitaxy results in perfectly commensurate, monocrystalline moiré supercrystals, which are distinctly different from conventional moiré superlattices. The high crystal quality of the 2D Cr₅Te₈ crystals is further confirmed by square magnetic hysteresis loops nearly free of defect pinning sites. The dative epitaxy is likely not limited to the present material systems and synthesis method, but should be applicable to a wide range of covalent materials on vdW templates, using a variety of thin film deposition techniques. This newly realized paradigm of thin film epitaxy not only is attractive for a plethora of industrial applications, but also offers opportunities to explore emergent phenomena in previously unattainable heterostructures.

4. Experimental Section

Synthesis of Cr₅Te₈/WSe₂ Heterostructures: Cr₅Te₈/WSe₂ heterostructures were synthesized through a two-step CVD process in a two-zone tube furnace with a 2 in. diameter. A schematic of the experimental setup and the heating profiles of the synthesis were shown in Figure S1b,c (Supporting Information). In the first step, WSe₂ monolayer was grown on sapphire or SiO₂/Si substrate. In a typical synthesis, 200 mg Se powder was placed in the first heating zone upstream of the furnace, which was kept at 400 °C during the growth. 5 mg WO₃ was mixed with 0.5 mg NaCl and loaded in the second heating zone downstream. Sapphire substrates were placed close to the WO₃ powder, while SiO₂/Si substrates were placed face down directly above the WO₃ powder. The second heating zone was heated with a ramping

rate of 20 °C min⁻¹ to the growth temperature of 820 °C and held at that temperature for 20 min before cooling down. During the growth process, the flow rate of 2% H₂/N₂ was kept at 80 standard cubic centimeters (sccm), and the growth was at ambient pressure. In the second step, the as-grown WSe₂ was used as the template for the epitaxial growth of 2D Cr₅Te₈ crystals to obtain Cr₅Te₈/WSe₂ heterostructures. 40 mg Te powder was placed in the first heating zone and ramped to 540 °C at a rate of 13 °C min⁻¹, and kept at 540 °C for 10 min. 1.2 mg CrCl₃ powder was placed in the second heating zone, and heated to 600 °C at a rate of 15 °C min⁻¹. The growth time was fixed at 10 min. A gas mixture containing 90% Ar and 10% H₂ with a flow rate of 100 sccm was used to carry the precursor vapor species to the substrate. Once the reaction ended, the furnace was cooled down naturally to room temperature.

The CVD growth of 2D Cr₅Te₈ crystals on WSe₂ template was dictated by monomer adsorption, desorption, and surface diffusion, as seen in Figure 1a. The weak bonding between the monomer and the WSe₂ vdW template led to low barriers for surface diffusion.^[26] The monomers aggregated to form nuclei. Once a nucleus reached a critical size,^[26a] the growth proceeded primarily by surface diffusion of monomers and their attachment to the edges of the nucleated 2D islands.^[26b] For Cr₅Te₈, the intralayer covalent bonding was substantially stronger than the interlayer bonding due to the presence of ordered vacancies. Such bonding character resulted in stronger adsorption energy of the monomers at the edges than that on the top surfaces. Together with ease of diffusion of monomers on the surface of WSe₂, atomically thin Cr₅Te₈ crystals could be achieved.^[26b]

The Cr₅Te₈/WSe₂ heterostructures with relatively thick (≈10 nm) and thin (1.4–2.8 nm) Cr₅Te₈ crystals were achieved by controlling the distance between the CrCl₃ precursor and the substrate, being ≈0.2 mm for the samples shown in Figure 1e and ≈2 mm for the ones in Figure 1f. Due to the high melting point (1150 °C) of CrCl₃, a steep vapor concentration gradient was established at the growth temperature of 600 °C. At a large precursor–substrate distance, the vapor concentration could be kept below the threshold of new nucleation on top of existing 2D layers, resulting in atomically thin Cr₅Te₈ crystals.

Interestingly, the 2D Cr₅Te₈ crystals deposited highly selectively on WSe₂ only, leaving sporadic nanocrystals on sapphire, as seen in Figure 1d. The absence of 2D crystal growth on these substrates was attributed to the covalent bonding and thus large surface diffusion barrier for monomers. This led to 3D growth of nanoparticles which eventually dewetted due to surface tension.

Film Transfer: The as-grown Cr₅Te₈/WSe₂ heterostructures were transferred onto TEM grids by dry transfer in a glove box with a nitrogen atmosphere. The Cr₅Te₈/WSe₂ heterostructures on SiO₂/Si substrate were first covered by poly(methyl methacrylate) (PMMA).^[27] After baking at 80 °C for 5 min, the PMMA film with Cr₅Te₈/WSe₂ heterostructures was peeled off from the SiO₂/Si substrate and then transferred to a TEM grid in a homebuilt alignment stage integrated with an optical microscope, followed by 5 min baking at 80 °C. The PMMA was removed by immersing the sample in acetone for 30 min.

Cross-Sectional STEM Sample Preparation: The as-grown Cr₅Te₈/WSe₂ heterostructure was exposed to a nitrogen atmosphere and subsequently covered by graphite through a routine dry-transfer method in the glove box to protect the surface from being oxidized. The cross-section STEM sample was prepared by using focused ion beam milling. It was thinned down to 70 nm thick at an accelerating voltage of 30 kV with a decreasing current from 0.79 nA to 80 pA, followed by a fine polish at an accelerating voltage of 2 kV with a small current of 21 pA to remove the amorphous layer.

HAADF-STEM Characterization: The atomically resolved HAADF-STEM images were carried out on an aberration-corrected scanning transmission electron microscope (FEI Tian Themis 60-300kV, operated at 300 kV). This transmission electron microscope is equipped with a double spherical-aberration corrector (DCOR) and a high-brightness field-emission gun (X-FEG) with a monochromator. The inner and outer collection angles for the STEM images (β_1 and β_2) were 38 and 200 mrad, respectively, with a semiconvergence angle of 30 mrad.

Cross-Sectional STEM Imaging: The cross-sectional HAADF-STEM revealed a clear vdW-like gap between the Cr₅Te₈ and WSe₂ layers, as shown in Figure S4h (Supporting Information), but Cr sites were nearly invisible due to strong scattering of Te which had a much larger atomic weight. To reveal the position of Cr, iDPC imaging was adopted, which measured the projected electrostatic potential instead of the integrated scattering signal of the atomic column.

STEM–EELS Characterization: EELS was acquired in the STEM mode and collected by setting the energy resolution to 1 eV at full width at half maximum of the zero-loss peak. The dispersion used was 0.5 eV per channel. EELS was acquired in the dual EELS mode to eliminate any systematic error due to the drift of the zero-loss peak.

STEM–EDS Characterization: Energy-dispersive X-ray spectroscopy (EDS) was acquired in STEM mode with a ChemiSTEM technology (X-FEG and SuperX EDS with four windowless silicon drift detectors) operated at 300 kV.

Raman and Photoluminescence (PL) Spectra: Raman and photoluminescence spectra were measured using a confocal Renishaw inVia Raman microscope equipped with a 514 nm laser. A 50× objective lens was used to focus the excitation lasers onto the sample and collect the emitted signals.

X-ray Diffraction (XRD) Spectrum: A Rigaku Ultima IV XRD system with an operational X-ray tube power of 1.76 kW (40 kV, 44 mA) and Cu target source was used. The XRD measurements were performed under $\theta/2\theta$ scanning mode and continuous scanning type with a step size of 0.02.

X-ray Photoelectron Spectroscopy (XPS) Spectrum: XPS was conducted on a PHI 5000 Versaprobe system using Al K α X-ray radiation for excitation.

DFT-Based Ab Initio Calculations: Density functional theory (DFT)-based ab initio calculations were performed by using the Vienna ab initio Simulation Package package. The Perdew–Burke–Ernzerhof form of the exchange correlation functional was used. Slab calculations were performed using supercell approach with a vacuum layer of ≈ 15 Å (to remove interaction between periodically repeated layers). The supercell was constructed using the observed moiré superlattice. The in-plane lattice constant of moiré superlattice was set at 23.3 Å. A plane-wave cutoff energy of 400 eV, and $4 \times 4 \times 1$ Monkhorst–Pack k -point mesh were used. The atomic positions were optimized by the conjugate gradient method to have all forces less 10^{-2} eV Å⁻¹. Spin–orbit was added after the relaxation accuracy was achieved. The zero damping DFT-D3 method of Grimme modeled the van der Waals interactions.

RMCD Measurements: The samples for RMCD measurements were capped with 2 nm Al by sputter deposition to prevent oxidation. The RMCD was defined as $(I_{\sigma^+} - I_{\sigma^-}) / (I_{\sigma^+} + I_{\sigma^-})$, where the $I_{\sigma^{\pm}}$ are the intensities of the reflected right and left circularly polarized light. RMCD measurements were performed with the sample mounted on a custom microscope/nanopositioner probe that was loaded into the variable-temperature helium insert of a 7 T magneto-optical cryostat (Oxford Instruments Spectramag). Light from a 633 nm HeNe laser was linearly polarized, and then modulated between left- and right-circular polarization at 50 kHz using a photoelastic modulator, before being focused to a 1 μ m diameter spot on the sample. Light reflected from the sample was detected by an avalanche photodiode, and the normalized difference between the two polarizations was measured using a lock-in amplifier.

XMCD Measurements: X-ray magnetic circular dichroism (XMCD) measurements were performed at Beamline 11.0.1 of the Advanced Light Source at the Lawrence Berkeley National Laboratory.

MRI-1726303, CBET-1510121), and the University at Buffalo VPRED seed grant. M.B. and Y.H. acknowledge support from the National Key R&D Program of China (Grant No. 2017YFA0206301), the National Natural Science Foundation of China (Grant Nos. 52027801, 51631001, 52101280), the China–German Collaboration Project (Grant No. M-0199), and the China Postdoctoral Science Foundation (Grant No. 2020M670042). L.Z. and J.L. acknowledge the support from the National Natural Science Foundation of China (Grant No. 11974156), the Guangdong International Science Collaboration Project (Grant No. 2019A050510001), the Science, Technology and Innovation Commission of Shenzhen Municipality (Grant No. ZDSYS20190902092905285), and also the assistance of SUSTech Core Research Facilities. J.C. and S.A.C. acknowledge the support from the National Science Foundation (Grant No. DMR-1644779), the State of Florida, and the U.S. Department of Energy. X.W. and X.M.C. acknowledge the support from the US National Science Foundation (Grant No. DMR-1708790). S.Z. acknowledges the support from the Grant No. NSF ECCS-2042126. R.F.S. acknowledges the support from the NU Collaborative Research and NSF-DMREF (Grant No. 1729288). This research used resources of the Advanced Light Source, which is a DOE Office of Science User Facility under contract no. DE-AC02-05CH11231.

Note: The acknowledgements were updated on April 27, 2022, after initial publication online.

Conflict of Interest

The authors declare no conflict of interest.

Author Contributions

M.B. and L.Z. contributed equally to this work. Y.H. and H.Z. conceived the project. J.L., Y.H., and H.Z. supervised the project. M.B., C.H., and A.M. prepared the Cr₅Te₈/WSe₂, Cr₅Te₈, and WSe₂ samples. L.Z. and Q.Y. transferred the samples and L.Z. performed the HAADF-STEM, EDS, and EELS characterizations. J.C. and S.A.C. performed the RMCD measurements. X.W. and R.V.C. performed the XMCD measurements. R.F.S. performed the first-principle calculations. M.B. performed the XRD, Raman, PL, and AFM measurements. Y.C.L. performed the XPS measurements. M.B., R.F.S., S.Z., J.L., Y.H., and H.Z. wrote the paper. All authors discussed the results and commented on the paper.

Data Availability Statement

The data that support the findings of this study are available from the corresponding author upon reasonable request.

Keywords

commensurate lattices, dative bonds, epitaxy, moiré superlattices, van der Waals interaction

Received: January 5, 2022

Revised: February 28, 2022

Published online: March 22, 2022

Supporting Information

Supporting Information is available from the Wiley Online Library or from the author.

Acknowledgements

M.B., C.H., A.M., and H.Z. acknowledge support from the US National Science Foundation (Grant Nos. ECCS-2042085, MRI-1229208,

- [1] a) R. Ribeiro-Palau, C. Zhang, K. Watanabe, T. Taniguchi, J. Hone, R. D. Cory, *Science* **2018**, 361, 690; b) W. J. Yu, Z. Li, H. Zhou, Y. Chen, Y. Wang, Y. Huang, X. Duan, *Nat. Mater.* **2013**, 12, 246; c) T. Georgiou, R. Jalil, B. D. Belle, L. Britnell, R. V. Gorbachev, S. V. Morozov, Y.-J. Kim, A. Gholinia, S. J. Haigh, O. Makarovsky, L. Eaves, L. A. Ponomarenko, A. K. Geim, K. S. Novoselov, A. Mishchenko, *Nat. Nanotechnol.* **2013**, 8, 100.

- [2] a) L. Britnell, R. M. Ribeiro, A. Eckmann, R. Jalil, B. D. Belle, A. Mishchenko, Y. J. Kim, R. V. Gorbachev, T. Georgiou, S. V. Morozov, A. N. Grigorenko, A. K. Geim, C. Casiraghi, A. H. C. Neto, K. S. Novoselov, *Science* **2013**, *340*, 1311; b) F. Withers, O. Del Pozo-Zamudio, A. Mishchenko, A. P. Rooney, A. Gholinia, K. Watanabe, T. Taniguchi, S. J. Haigh, A. K. Geim, A. I. Tartakovsky, K. S. Novoselov, *Nat. Mater.* **2015**, *14*, 301.
- [3] a) A. Avsar, H. Ochoa, F. Guinea, B. Özyilmaz, B. J. van Wees, I. J. Vera-Marun, *Rev. Mod. Phys.* **2020**, *92*, 021003; b) J. F. Sierra, J. Fabian, R. K. Kawakami, S. Roche, S. O. Valenzuela, *Nat. Nanotechnol.* **2021**, *16*, 856; c) Y. Ou, W. Yanez, R. Xiao, M. Stanley, S. Ghosh, B. Zheng, W. Jiang, Y. Huang, T. Pillsbury, A. Richardella, C. Liu, T. Low, V. H. Crespi, K. A. Mkhoyan, N. Samarth, arXiv: 2107.08599, **2021**.
- [4] a) C. Zhao, T. Norden, P. Zhang, P. Zhao, Y. Cheng, F. Sun, J. P. Parry, P. Taheri, J. Wang, Y. Yang, T. Scrace, K. Kang, S. Yang, G.-x. Miao, R. K. Sabirianov, G. Kioseoglou, W. Huang, A. Petrou, H. Zeng, *Nat. Nanotechnol.* **2017**, *12*, 757; b) D. Zhong, L. Seyler Kyle, X. Linpeng, R. Cheng, N. Sivasdas, B. Huang, E. Schmidgall, T. Taniguchi, K. Watanabe, A. McGuire Michael, W. Yao, D. Xiao, C. Fu Kai-Mei, X. Xu, *Sci. Adv.* **2017**, *3*, e1603113.
- [5] a) Y. Cao, V. Fatemi, S. Fang, K. Watanabe, T. Taniguchi, E. Kaxiras, P. Jarillo-Herrero, *Nature* **2018**, *556*, 43; b) L. Sharpe Aaron, J. F. Eli, W. B. Arthur, J. Finney, K. Watanabe, T. Taniguchi, M. A. Kastner, D. Goldhaber-Gordon, *Science* **2019**, *365*, 605; c) S. Huang, K. Kim, D. K. Efimkin, T. Lovorn, T. Taniguchi, K. Watanabe, A. H. MacDonald, E. Tutuc, B. J. LeRoy, *Phys. Rev. Lett.* **2018**, *121*, 037702; d) Y. Cao, V. Fatemi, A. Demir, S. Fang, S. L. Tomarken, J. Y. Luo, J. D. Sanchez-Yamagishi, K. Watanabe, T. Taniguchi, E. Kaxiras, R. C. Ashoori, P. Jarillo-Herrero, *Nature* **2018**, *556*, 80; e) Q. Tong, H. Yu, Q. Zhu, Y. Wang, X. Xu, W. Yao, *Nat. Phys.* **2017**, *13*, 356; f) M. Serlin, C. L. Tschirhart, H. Polshyn, Y. Zhang, J. Zhu, K. Watanabe, T. Taniguchi, L. Balents, A. F. Young, *Science* **2020**, *367*, 900.
- [6] a) B. Hunt, J. D. Sanchez-Yamagishi, A. F. Young, M. Yankowitz, B. J. LeRoy, K. Watanabe, T. Taniguchi, P. Moon, M. Koshino, P. Jarillo-Herrero, R. C. Ashoori, *Science* **2013**, *340*, 1427; b) C. R. Dean, L. Wang, P. Maher, C. Forsythe, F. Ghahari, Y. Gao, J. Katoch, M. Ishigami, P. Moon, M. Koshino, T. Taniguchi, K. Watanabe, K. L. Shepard, J. Hone, P. Kim, *Nature* **2013**, *497*, 598.
- [7] Y. Tang, L. Li, T. Li, Y. Xu, S. Liu, K. Barmak, K. Watanabe, T. Taniguchi, A. H. MacDonald, J. Shan, K. F. Mak, *Nature* **2020**, *579*, 353.
- [8] a) C. Jin, E. C. Regan, A. Yan, M. Iqbal Bakti Utama, D. Wang, S. Zhao, Y. Qin, S. Yang, Z. Zheng, S. Shi, K. Watanabe, T. Taniguchi, S. Tongay, A. Zettl, F. Wang, *Nature* **2019**, *567*, 76; b) K. L. Seyler, P. Rivera, H. Yu, N. P. Wilson, E. L. Ray, D. G. Mandrus, J. Yan, W. Yao, X. Xu, *Nature* **2019**, *567*, 66; c) Y. Shimazaki, I. Schwartz, K. Watanabe, T. Taniguchi, M. Kroner, A. Imamoğlu, *Nature* **2020**, *580*, 472; d) N. P. Wilson, W. Yao, J. Shan, X. Xu, *Nature* **2021**, *599*, 383.
- [9] L. Liu, J. Park, A. Siegel David, F. McCarty Kevin, W. Clark Kendal, W. Deng, L. Basile, C. Idrobo Juan, A.-P. Li, G. Gu, *Science* **2014**, *343*, 163.
- [10] a) T. Zhang, L. Fu, *Chem* **2018**, *4*, 671; b) Y. Gong, J. Lin, X. Wang, G. Shi, S. Lei, Z. Lin, X. Zou, G. Ye, R. Vajtai, B. I. Yakobson, H. Terrones, M. Terrones, B. K. Tay, J. Lou, S. T. Pantelides, Z. Liu, W. Zhou, P. M. Ajayan, *Nat. Mater.* **2014**, *13*, 1135; c) R. Wu, Q. Tao, W. Dang, Y. Liu, B. Li, J. Li, B. Zhao, Z. Zhang, H. Ma, G. Sun, X. Duan, X. Duan, *Adv. Funct. Mater.* **2019**, *29*, 1806611.
- [11] a) A. Koma, K. Sunouchi, T. Miyajima, *Microelectron. Eng.* **1984**, *2*, 129; b) K. Reidy, G. Varnavides, J. D. Thomsen, A. Kumar, T. Pham, A. M. Blackburn, P. Anikeeva, P. Narang, J. M. LeBeau, F. M. Ross, *Nat. Commun.* **2021**, *12*, 1290; c) A. Koma, *Thin Solid Films* **1992**, *216*, 72.
- [12] D. Liang, T. Wei, J. Wang, J. Li, *Nano Energy* **2020**, *69*, 104463.
- [13] W. Xie, T.-M. Lu, G.-C. Wang, I. Bhat, S. Zhang, *Phys. Rev. Mater.* **2017**, *1*, 063402.
- [14] a) N. R. Wilson, P. V. Nguyen, K. Seyler, P. Rivera, A. J. Marsden, Z. P. L. Laker, G. C. Constantinescu, V. Kandyba, A. Barinov, N. D. M. Hine, X. Xu, D. H. Cobden, *Sci. Adv.* **2017**, *3*, e1601832; b) G. C. Constantinescu, N. D. M. Hine, *Phys. Rev. B* **2015**, *91*, 195416.
- [15] a) M. Bian, A. N. Kamenskii, M. Han, W. Li, S. Wei, X. Tian, D. B. Eason, F. Sun, K. He, H. Hui, F. Yao, R. Sabirianov, J. P. Bird, C. Yang, J. Miao, J. Lin, S. A. Crooker, Y. Hou, H. Zeng, *Mater. Res. Lett.* **2021**, *9*, 205; b) X. Zhao, P. Song, C. Wang, A. C. Riis-Jensen, W. Fu, Y. Deng, D. Wan, L. Kang, S. Ning, J. Dan, T. Venkatesan, Z. Liu, W. Zhou, K. S. Thygesen, X. Luo, S. J. Pennycook, K. P. Loh, *Nature* **2020**, *581*, 171.
- [16] J. Zhou, X. Kong, M. C. Sekhar, J. Lin, F. Le Goualher, R. Xu, X. Wang, Y. Chen, Y. Zhou, C. Zhu, W. Lu, F. Liu, B. Tang, Z. Guo, C. Zhu, Z. Cheng, T. Yu, K. Suenaga, D. Sun, W. Ji, Z. Liu, *ACS Nano* **2019**, *13*, 10929.
- [17] Y. Liu, C. Zeng, J. Yu, J. Zhong, B. Li, Z. Zhang, Z. Liu, Z. M. Wang, A. Pan, X. Duan, *Chem. Soc. Rev.* **2021**, *50*, 6401.
- [18] J. Taheri, J. Wang, H. Xing, J. F. Destino, M. M. Arik, C. Zhao, K. Kang, B. Blizzard, L. Zhang, P. Zhao, S. Huang, S. Yang, F. V. Bright, J. Cerne, H. Zeng, *Mater. Res. Express* **2016**, *3*, 075009.
- [19] J. Narayan, B. C. Larson, *J. Appl. Phys.* **2002**, *93*, 278.
- [20] C. Chen, X. Chen, C. Wu, X. Wang, Y. Ping, X. Wei, X. Zhou, J. Lu, L. Zhu, J. Zhou, T. Zhai, J. Han, H. Xu, *Adv. Mater.* **2021**, *34*, 2107512.
- [21] W. Tang, E. Sanville, G. Henkelman, *J. Phys.: Condens. Matter* **2009**, *21*, 084204.
- [22] D. H. Pearson, C. C. Ahn, B. Fultz, *Phys. Rev. B* **1993**, *47*, 8471.
- [23] a) T. Sohler, E. Ponomarev, M. Gibertini, H. Berger, N. Marzari, N. Ubrig, A. F. Morpurgo, *Phys. Rev. X* **2019**, *9*, 031019; b) W. Zhao, Z. Ghorannevis, K. K. Amara, J. R. Pang, M. Toh, X. Zhang, C. Kloc, P. H. Tan, G. Eda, *Nanoscale* **2013**, *5*, 9677.
- [24] R. Mondal, R. Kulkarni, A. Thamizhavel, *J. Magn. Magn. Mater.* **2019**, *483*, 27.
- [25] a) A. L. Coughlin, D. Xie, X. Zhan, Y. Yao, L. Deng, H. Hewa-Walpitage, T. Bontke, C.-W. Chu, Y. Li, J. Wang, H. A. Fertig, S. Zhang, *Nano Lett.* **2021**, *21*, 9517; b) D. Zhao, L. Zhang, I. A. Malik, M. Liao, W. Cui, X. Cai, C. Zheng, L. Li, X. Hu, D. Zhang, J. Zhang, X. Chen, W. Jiang, Q. Xue, *Nano Res.* **2018**, *11*, 3116.
- [26] a) J. Zhou, Y. Yang, Y. Yang, D. S. Kim, A. Yuan, X. Tian, C. Ophus, F. Sun, A. K. Schmid, M. Nathanson, H. Heinz, Q. An, H. Zeng, P. Ercius, J. Miao, *Nature* **2019**, *570*, 500; b) K. Zhang, C. Ding, B. Pan, Z. Wu, A. Marga, L. Zhang, H. Zeng, S. Huang, *Adv. Mater.* **2021**, *33*, 2105079.
- [27] P. Wang, S. Song, A. Najafi, C. Huai, P. Zhang, Y. Hou, S. Huang, H. Zeng, *ACS Nano* **2020**, *14*, 7370.